Nephrol Dial Transplant (2012) 27: 358–368
doi: 10.1093/ndt/gfr342
Advance Access publication 18 July 2011

Disturbed flow in radial-cephalic arteriovenous fistulae for haemodialysis: low and oscillating shear stress locates the sites of stenosis

Bogdan Ene-Iordache[1] and Andrea Remuzzi[1,2]

[1]Department of Biomedical Engineering, Laboratory of Biomedical Technologies, Mario Negri Institute for Pharmacological Research, Ranica, Italy and [2]Department of Industrial Engineering, University of Bergamo, Dalmine, Italy

Correspondence and offprint requests to: Bogdan Ene-Iordache; E-mail:bogdan@marionegri.it

Abstract

Background. Despite recent clinical and technological advancements, the vascular access (VA) for haemodialysis still has significant early failure rates after arteriovenous fistula (AVF) creation. VA failure is mainly related to the haemodynamic conditions that trigger the phenomena of vascular wall disease such as intimal hyperplasia (IH) or atherosclerosis.

Methods. We performed transient computational fluid dynamics simulations within idealized three-dimensional models of 'end-to-side' and 'end-to-end' radio-cephalic anastomosis, using non-Newtonian blood and previously measured flows and division ratio in subjects requiring primary access procedure as boundary conditions.

Results. The numerical simulations allowed full characterization of blood flow inside the AVF and of patterns of haemodynamic shear stress, known to be the major determinant of vascular remodelling and disease. Wall shear stress was low and oscillating in zones where flow stagnation occurs on the artery floor and on the inner wall of the juxta-anastomotic vein.

Conclusions. Zones of low and oscillatory shear stress were located in the same sites where luminal reduction was documented in previous experimental studies on sites stenosis distribution in AVF. We conclude that even when exposed to high flow rates, there are spot regions along the AVF exposed to athero-prone shear stress that favour vessel stenosis by triggering IH.

Keywords: arteriovenous fistula; computational fluid dynamics (CFD); intimal hyperplasia; vascular access; wall shear stress

Introduction

Forty-five years after the first radiocephalic arteriovenous fistula (AVF) performed by Dr Appell in New York [1], maintaining adequate long-term vascular access (VA) for chronic haemodialysis patients needing renal replacement therapy is one of the most difficult problems vascular surgeons or nephrologists face. A newly created fistula must mature in order for it to be used for dialysis, that is, the artery and vein must remodel to accommodate the markedly increased blood flow that results from creating the arteriovenous anastomosis. Then, the lifetime of a VA can range between months or several years until the fistula stops functioning for adequate haemodialysis, requiring surgical revision.

Mechanisms underlying fistula early-maturation failure have been studied for years. Anatomic factors such as diameter or intimal thickness of feeding artery and draining vein were shown to be important predictors for AVF maturation, while non-anatomic factors that are involved in maturation failure include the haemodynamic stresses (altered shear stress and venous hypertension) that result from creating a VA anastomosis or underlying vascular pathology like impaired endothelial function associated with chronic kidney disease or diabetes [2]. Measures for the problem resolution were proposed [3, 4] but the VA failure rate continues to remain high [5]. To have an idea of the actual VA problems, it is worth knowing that in Dr Appell's first series of surgically created fistulas there were only 2 failures out of 14, that is an early failure rate which would be difficult to achieve even today [6].

The haemodynamic conditions play a fundamental role in regulating the vascular structure. Blood flow regulates arterial diameter through changes in wall shear stress (WSS), and intraluminal pressure regulates artery wall thickness through its effect on wall tension. If different from the normal physiological range, namely in 'disturbed flow' conditions, these haemodynamic factors are implicated in the aetiology of the vascular wall disease. The physiological magnitude of WSS ranges from 10 to 70 dyne/cm^2 in normal arteries, while outside this range WSS can trigger mechanisms that lead to vascular pathology. Lower values of WSS may induce atherosclerotic plaques formation and therefore are considered 'atherosclerosis prone', while WSS higher than this range may provoke endothelial cells cleavage and consequently 'high-shear' induced thrombosis [7]. More recently, it was clarified that disturbed flow is a condition of endothelium exposed to low average shear stress, constantly changing gradients of shear stress, oscillatory shear stress and multidirectional secondary flows. These haemodynamic conditions occur in specific sites of the arterial tree where

there is blood flow separation or stagnation points like the arterial branches, at stenosed sites or around stent struts [8].

The main cause of VA failure is thrombosis secondary to the development of stenosis, which in turn is caused by intimal hyperplasia (IH), a fibro-muscular thickening of the vessel wall [9, 10]. Previous studies have shown that in AVF for haemodialysis, the stenoses occur in specific sites. In 'end-to-side' AVF, Sivaneasn *et al.* [11] classified the stenoses developed at the anastomosis floor as Type 1, on the inner wall of the swing segment (the vein part mobilized in the creation of the anastomosis) as Type 2 and after the curved region when the vein straightens out as Type 3. Badero *et al.* [12] found that the stenoses occur mostly on the swing segment, with the juxta-anastomotic as the most predominant site.

Also in IH, the haemodynamic shear stress seems to be the trigger factor, especially the low WSS at stagnation points [13]. WSS is difficult to assess because it represents physically the stress (e.g. average force per unit area) vector exerted by flowing blood tangential to the endothelium, with a magnitude equal to the product between shear rate (the derivative of the blood velocity profile near the vessel wall) and blood viscosity. Previous studies on AVF maturation failure that have addressed the issue of haemodynamic forces that develop inside the AVF often used a simplified model (e.g. Poiseuille) for shear stress calculation [14, 15] yielding only a rough estimation of the averaged WSS. Computational fluid dynamics (CFD) are numerical techniques that allow proper calculation of the spatial distribution of WSS among other haemodynamic variables of interest, like for example velocity field and pressure. Since the 90s, numerical modelling on idealized geometries was intensively used to assess WSS in studying the link between haemodynamics and cardiovascular disease, like stenosis development in the carotid bifurcation [16, 17] the aortic arch [18, 19] or bypass anastomoses [20, 21]. Such computational studies helped to better understand the haemodynamic phenomena on simplified models and introduced new concepts like the role of low WSS in triggering atherosclerosis [22], oscillatory shear index [16, 23], that overthrew the study of vascular diseases and were further transferred in patient-specific studies [24]. Despite its clinical relevance, this type of investigational method was less used for the study of VA complications. With respect to the literature on carotid and coronary arteries, there were relatively few papers that addressed this task by means of numerical modelling and all were published after the 2000s [25–32]. Beside haemodynamics evaluation, CFD has been validated against particle image velocimetry [30] and with *in vitro* flow measurements [31] confirming the validity of these techniques in the VA setting as well.

Overall, the VA is a very high-blood flow rate conduit with respect to the physiological condition, but whether low WSS develops in these areas is not well elucidated. Similar to the above-mentioned studies [16–21] in other vascular segments affected by stenosis development, numerical studies on idealized models can characterize the general flow and WSS patterns that develop after the surgical creation of AVF if proper dimensional modelling and boundary conditions are employed. With this aim, we used pulsatile CFD simulations in idealized models of the AVF created at the wrist as VA for haemodialysis patients.

Materials and methods

Three-dimensional models of the AVF

There is now widespread agreement in the scientific community on whether the native subcutaneous AVF is the best choice with which we are acquainted for achieving VA for haemodialysis [33, 34]. The end-vein-to-side-artery (end-to-side) anastomosis at the wrist between the cephalic vein and radial artery is the most common technique performed in VA, although some groups prefer the 'end-to-end' technique. The original Brescia-Cimino anastomoses of type 'side-to-side' [1] are less used today, even though they are well indicated in patient cases with stiffer arm vessels [5]. For this reason, in the present study, we only considered the end-to-side and end-to-end connections between the cephalic vein and the radial artery performed at the wrist. End-to-side fistulas are created by suturing the transected end of the cephalic vein to the side of the radial artery. In case of end-to-end AVF, both artery and vein are resected and the radial artery is curved at 180° to form an U-shaped bend before suturing the anastomosis [5]. In designing idealized models of end-to-side and end-to-end AVF, we were inspired by the drawings of surgical anastomoses presented by Konner [5, 35] as shown in Figure 1a and b.

For the end-to-side AVF model, we considered the geometrical parameters measured by Sivanesan *et al.* [11] at 1-day post-operatively. Vessel diameters were 3.1 and 4.1 mm for the radial artery and cephalic vein, respectively, and the anastomotic angle was 49°. The extent of the proximal artery (PA) and distal artery (DA) and of the vein was assumed 12 times the vein diameter in order to have enough hydraulic length to allow fully developed flow. The bend zone of the cephalic vein was generated with a curvature radius that is 2-fold the vessel diameter. For the end-to-end AVF, we used data from our previous study [36] where vessel diameters were measured pre- and then up to 3 months post-operatively. The radial artery diameter was 3.7 mm and that of the vein was 5.0 mm corresponding to 7-day post-operative condition. The length of the artery was 14 and of the vein 10 vein diameters, and the 180° bending zone was realized with a curvature radius equal to two artery diameters. For both AVF models, tapering of the juxta-anastomosis vein for a length equal to two diameters was created to ensure smooth transition between artery (smaller) to vein (greater) section.

Three-dimensional (3-D) grids of AVF made of eight-node hexahedral elements, with a boundary layer of thinner elements near the wall, were created using a pre-processor meshing program (GAMBIT; Fluent Inc, Lebanon, NH). The schematic models of AVF and corresponding three-dimensional meshes for CFD are presented in Figure 1c–f.

Numerical simulations of blood flow in the AVF

For the end-to-side fistula, two types of flow may exist in the DA: retrograde, when blood flows toward the anastomosis and antegrade, when blood flows toward the hand. For the unsteady simulations, we used the cephalic vein flow rate waveform provided in [37], opportunely scaled to yield a time-averaged flow rate equal to the flow rate measured by the same authors in their previous study [38] aimed at characterizing the flow distributions at 1-day post-operatively. Blood volume flow waveform in the radial artery for the end-to-end AVF simulation was taken from [36] for the 7-day post-operative condition. The three pulse cycle waveforms are presented in Figure 2 and the flow characteristics together with the geometrical parameters of the AVF mesh models are summarized in Table 1.

3-D pulsatile flow simulations in the AVF models were computed using a multipurpose CFD package (FIDAP; Fluent Inc, Lebanon, NH) based on the finite element method. As boundary conditions, fully developed parabolic velocities at the vein outlet and at PA inlet (V and PA in Figure 1) were prescribed for end-to-side AVF and at the artery inlet only for end-to-end AVF, with centre-line velocities derived from the flow waveforms previously reported. Traction-free boundary condition was applied at the DA outlet for end-to-side and to vein outlet for end-to-end AVF to ensure conservation of mass and no-slip condition (i.e. zero velocity) was applied at the walls, which were considered rigid. We employed an implicit time integration scheme (backward Euler) with 50 fixed time steps for each pulse cycle to solve the time-dependent Navier–Stokes equations, assuming that cardiac cycle period is 1 s. Three complete flow cycles were solved in order to damp the initial transients of the fluid and

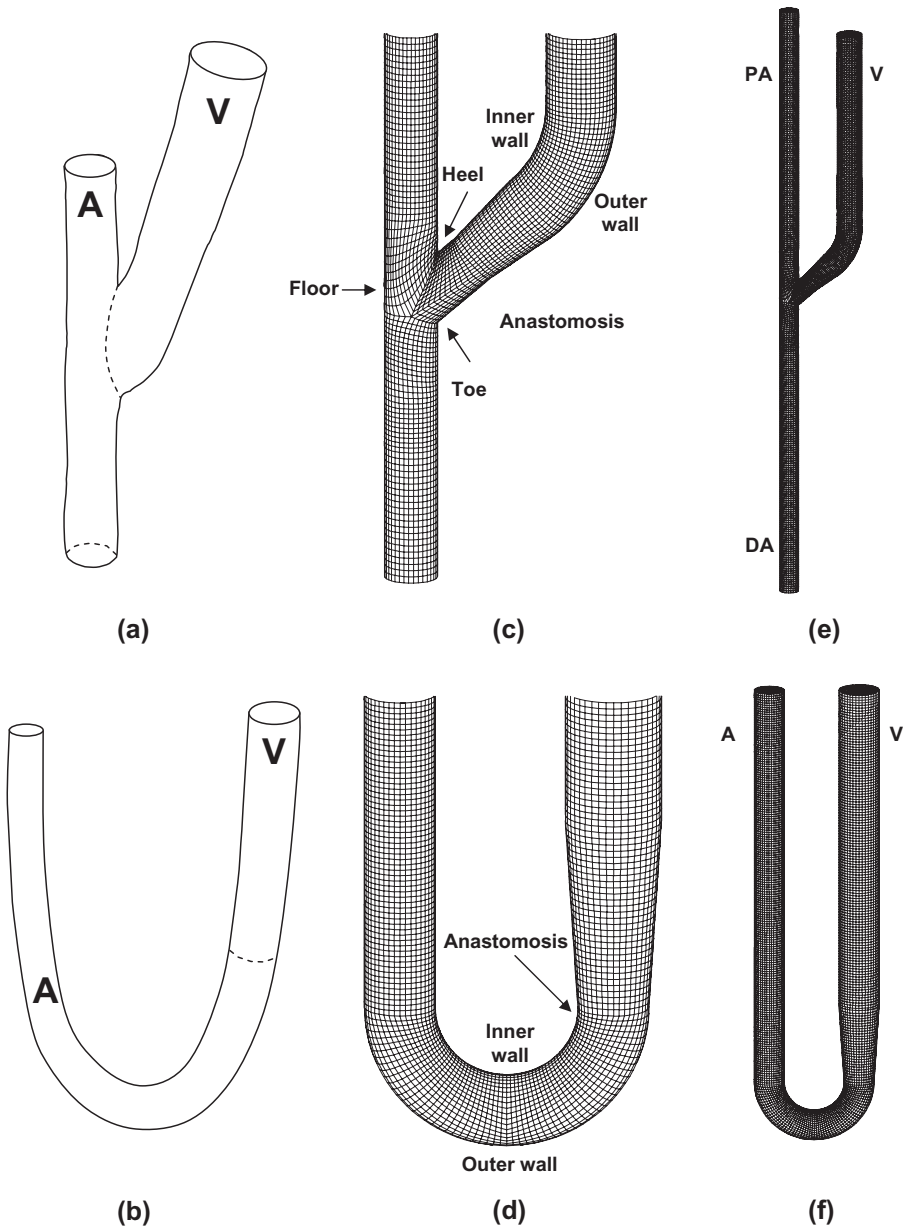

Fig. 1. 'End-to-side' (top row) and 'end-to-end' (bottom row) models of radial-cephalic anastomosis for vascular access at the wrist. (**a**) and (**b**) Schematic drawings of the AVF used as models. (**c**) and (**d**) Zoom on 3-D meshes near the anastomotic region. (**e**) and (**f**) 3-D meshes for numerical simulations. Drawings of the AVF were adapted from [5]. Legend: A, artery (radial); V vein (cephalic); PA, proximal artery; DA, distal artery.

only the third cycle was considered for the final results. Blood density was assumed constant (1.045 g/cm^3) and blood viscosity was considered non-Newtonian by using the Carreau rheological model implemented in the CFD package as described previously [25]. Since blood viscosity depends on the shear rate, Reynolds number cannot be calculated directly, but a good approximation can be made by rescaling the Newtonian viscosity to a value corresponding to a characteristic shear rate [39]. For the outlet vein of end-to-side and the inlet artery of end-to-end AVF, we calculated the Reynolds number as described in [25] and the resulting mean and ranges are provided in Table 1.

The oscillatory shear index (OSI), originally introduced by Ku *et al.* [16], is aimed at quantifying the degree of deviation of the WSS from its average direction during the heart beat cycle due to either secondary and reverse flow velocity components occurring in pulsatile flow. In order to estimate whether oscillatory shear might occur on the AVF wall, for each point on the surface, we calculated the OSI as proposed in [23]:

$$\mathrm{OSI} = \frac{1}{2}\left(1 - \frac{|\int_0^T \tau_w \, dt|}{\int_0^T |\tau_w| \, dt}\right),$$

where $\tau_w(t)$ is the instantaneous WSS vector and T is the period of the cardiac cycle. The index is non-dimensional and can take values between 0 and 0.5, higher OSI indicating larger shear stress direction variations.

Himburg *et al.* [40] introduced another indicator of the 'disturbed' shear environment, namely the relative residence time (RRT) of non-adherent particles in the blood flow moving adjacent to the vascular wall. They showed that RRT of a fully entrained particle at a small distance from the wall is inversely proportional with the distance the particle travels during a cardiac cycle, which may be expressed as a combination of OSI and time-averaged WSS (TAWSS) over the cardiac cycle. For each node on the AVF mesh surface, we calculated the RRT with the formula [40]:

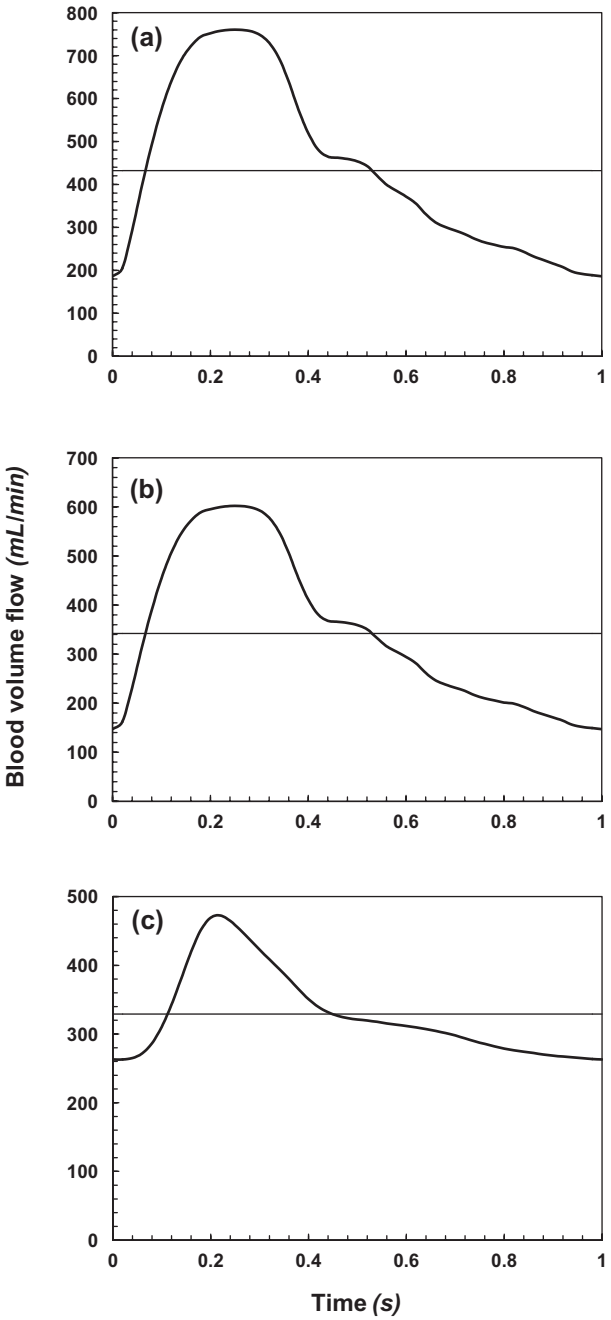

Fig. 2. Blood volume flow waveforms used in pulsatile CFD simulations. The horizontal line indicates the time-averaged blood flow rate over the cardiac cycle. Downstream arterial resistance was calculated as resistive index = (peak systolic flow − minimum diastolic flow)/peak systolic flow. (**a**) Venous outflow waveform used for the 'end-to-side' AVF with retrograde flow in the DA (mean 432 mL/min, resistive index = 0.75). (**b**) Venous outflow waveform used for the end-to-side AVF with antegrade flow in the DA (mean 342 mL/min, resistive index = 0.75). (**c**) Arterial inflow waveform used for the 'end-to-end' AVF (mean 329 mL/min, resistive index = 0.44).

$$\mathrm{RRT} \sim [(1-2 \cdot \mathrm{OSI}) \cdot \mathrm{TAWSS}]^{-1}.$$

In this formulation, OSI acts to modify the effect of TAWSS on the relative residence of particles near the wall and thus RRT incorporates information on both low and oscillating shear [40]. The RRT must be normalized by a reference value [24], which we chose to be the RRT calculated for fully developed, time-averaged blood volume flow in the straight part of the vein for each AVF. After this transformation, an RRT value near 1 indicates a condition of shear environment similar to the reference RRT, while RRT <1 indicates high shear zones and RRT >1 locates the sites with both low and oscillating shear stress or areas with only low WSS.

Results

Flow patterns in the AVF

Velocity contours of blood in the symmetry section of the end-to-side for the retrograde and antegrade flow in DA cases are shown in Figure 3a and b for the peak systolic and Figure 3d and e for the minimum diastolic blood volume flow. In retrograde flow in DA (Figure 3a and d), blood that comes mostly (74% of flow) from the PA and in a smaller fraction (26%) from the DA enters through the anastomosis into the cephalic vein. This type of blood distribution between the proximal and DA creates a flow stagnation zone (A) on the anastomosis floor as depicted by the white streamlines. A region of flow recirculation forms near the heel in the juxta-anastomosis vein, when the flow hits on the outer wall of the vein forming a counterclockwise vortex on the opposite inner wall (B). In antegrade flow in DA (Figure 3b and e) blood flows from the PA toward the anastomosis where it divides: the greater part of the flow enters into the vein (81%) and only a smaller part flows through the DA (19%) toward the palmary arch. When blood reaches the anastomosis, the flow directed toward the DA changes direction suddenly creating a wider area of recirculation and low velocity on the floor, starting from the anastomosis down to the DA (A). The flow entering the vein collides against the outer wall near the anastomosis creating an area of recirculation flow on the inner wall near the heel (B). Flow patterns in retrograde and antegrade flow seem similar, except for the position A where a different shape of the flow recirculation region can be observed.

The sudden curvature of the vein limb of AVF near the anastomosis leads to the formation of Dean vortices characteristic for curved tubes. These can be well observed in the cross-sections normal to the vessel axis in position B, as shown in Figure 3a and b. The Dean flow type is well developed immediately near anastomosis and vanishes gradually after the vein bend.

Velocity magnitude plots of blood in the end-to-end AVF for peak systolic and minimum diastolic blood volume flow are shown in Figure 3c and f. In this case, whole blood coming from the radial artery flows through the cephalic vein in a U-shape tube. After the anastomosis, the flow impacts on the outer wall and a recirculation zone (C) develops on the inner wall of the juxta-anastomosis vein. Also in this case, the curvature of the artery induces Dean type flow in the bending tract of the AVF, as shown in the cross-section normal to the vessel axis in position B.

WSS patterns in the AVF

To assess how WSS patterns are distributed over the AVF surface, we represented the WSS magnitude with a cut-off

Table 1. Geometrical parameters and flow characteristics used in the CFD simulations[a]

		Diameter (mm)	Flow division ratio	Flow rate (mL/min)	Re number
End-to-side AVF					
Retrograde flow in DA	V	4.1	74% PA:26% DA:100% V	432 (760–186)	670 (1196–278)
	PA	3.1			
	DA	3.1			
Antegrade flow in DA	V	4.1	100% PA:19% DA:81% V	342 (602–147)	526 (941–217)
	PA	3.1			
	DA	3.1			
End-to-end AVF	A	3.7	100% A:100% V	329 (472–263)	563 (820–448)
	V	5.0			

[a]A, artery (radial); V, vein (cephalic); PA, proximal artery; DA, distal artery; Re, Reynolds number. Flow rates and Reynolds numbers are expressed as time-averged and (maximum–minimum) of the flow waveforms in Figure 2.

value of 70 dyne/cm^2 representing the maximum value in normal arteries [7] and eight levels of WSS patterns as shown in Figure 4. In this way, low WSS zones are plotted in dark blue (<10 dyne/cm^2) and high WSS (>70 dyne/cm^2) zones are in red. As shown, low WSS match well the sites of flow recirculation and stagnation presented in Figure 3. In particular, for end-to-side AVF, areas of low WSS are found along the wall of the anastomotic floor (A), near the anastomosis heel on the inner wall of the vein (B) and in a lesser extent on the inner wall (C) after the curvature of the vein. When the flow rate is maximum, the high WSS covers all surface of the PA as well as of the cephalic vein, except for the small focal sites on the inner side in point B and C on end-to-side AVF, while when the flow rate is at minimum, high WSS areas covered is only on the outer and lateral wall of the swing segment (see Figure 4a–e). WSS patterns on the PA and on the vein are very similar, but rather dissimilar on the DA, where area of low WSS (A) is wider in the antegrade flow in DA case with respect to the retrograde case. As the AVF geometries are identical, this diversity is due to the different flow distribution between the two cases. For end-to-end AVF, low WSS regions are presented on the inner wall of the cephalic vein (Position C), whereas high WSS develops on the inner and lateral walls of the bending artery in the peak systolic flow condition as shown in Figure 4c. These patterns are maintained at minimum diastolic blood volume flow but the highest WSS does not reach the limit of 70 dyne/cm^2 (Figure 4f).

It is worth noting from the shear stress patterns in Figure 4 that low and high WSS regions are present with different extent on the AVF surface in both maximum and minimum flow instances. We should imagine how these areas continue to fluctuate cyclically, from systole to diastole, with the heart frequency. It can be also observed that in all AVF, the Dean flow that develops in the curved tracts contribute to higher WSS on the lateral walls and lower WSS on the inner and outer walls that are normal with respect to the radius of curvature of the bend. This type of pattern can be well observed in the minimum diastolic blood volume flow condition in Figure 4d–f.

Surface maps of OSI are presented in Figure 5a–c. Zones of non-null OSI were found on the anastomosis floor (A) and near the heel on the inner wall (B) of the swing segment in end-to-side AVF (Figure 5a and b) and on the inner wall of the vein after the anastomosis (C) in end-to-end AVF (Figure 5c). In particular, the highest OSI were 0.31 in Position A and 0.075 in Position B of Figure 5a, 0.45 in Position A and 0.077 in Position B of Figure 5b and 0.29 in Position C of Figure 5c. The RRT contours mapped over the AVF model surface are presented in Figure 5d–f. As shown, the location of RRT on the wall is consistent with the distribution of OSI, but RRT patterns are more extended as they are caused either by elevated OSI or low TAWSS. Median values of RRT distributions were 0.67, 0.64 and 0.42, respectively from Figure 5d–f. Since RRT does not have a well-defined range for the visualization map scale, we chose the averaged 75% quintile of RRT distributions as lower limit and set the upper limit to the lowest maximum RRT, which is in Figure 5d. The peak RRT were 10.4 in Position A and 9.7 in Position B of Figure 5d, 54.6 in Position A and 4.6 in Position B of Figure 5e and 30.7 in Position C of end-to-end AVF in Figure 5f.

Discussion

In the present work, by employing pulsatile CFD simulations in idealized models with realistic blood volume flow conditions, we studied the shear environment in order to investigate whether disturbed flow occurs on the AVF territory. In particular, in idealized AVF, we found that low WSS (<10 dyne/cm^2) occurs at the anastomotic floor, on the inner wall of the swing segment and after the vein curvature in end-to-side and on the inner wall of the juxta-anastomotic vein in end-to-end AVF, in line with previous patient-specific CFD studies [25, 30, 32]. In all these sites, except for the venous outflow, we have found not only low but also oscillating WSS. Niemann *et al.* [31] found similar findings on the draining veins in a side-to-side AVF model. Our results also demonstrate that in end-to-side and end-to-end AVF for haemodialysis, exposed to post-operative sudden increase in blood volume flow and decrease of waveform pulsatility, there are regions of flow reversal producing oscillations in shear direction. Few authors reported oscillating WSS in the AVF for haemodialysis. Using OSI calculation based on axially directed WSS in cross-sections as defined in [18], we have shown non-null OSI on one perimeter slicing the swing segment [25], while a similar study [30] reported null OSI on several cross-sections considered, but none of these perimeters encompassed the flow separation zone on the inner side of the

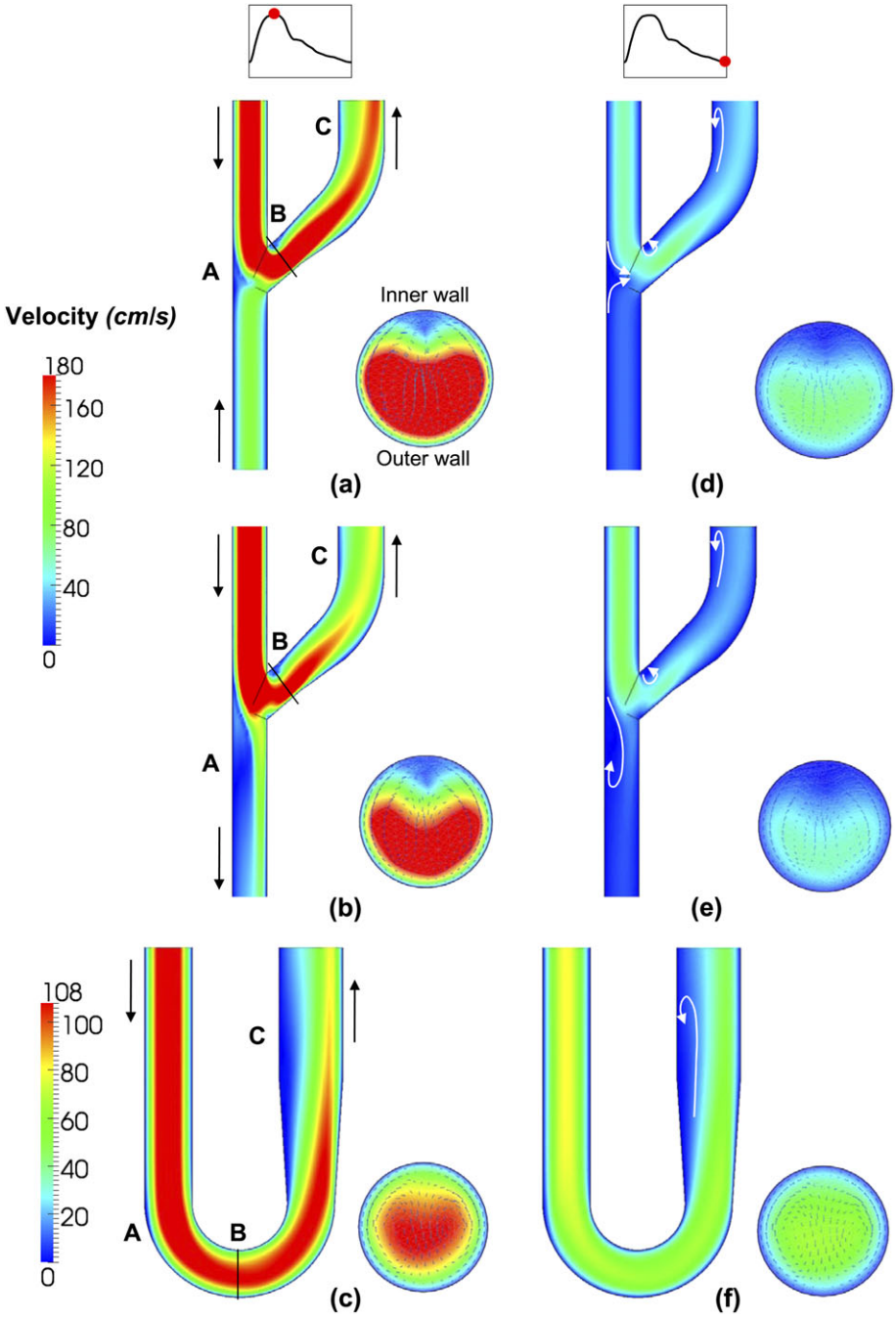

Fig. 3. Velocity magnitude contours of blood in the symmetry plane of the AVF and in a cross-section (B) of the bending vessel. (**a–c**) Velocity maps corresponding to maximum blood flow rates. (**d–f**) Velocity maps for the minimum blood volume flow. (**a** and **d**) 'End-to-side' AVF case with retrograde flow in the DA. (**b** and **e**) End-to-side AVF case with antegrade flow in the DA. (**c** and **f**). 'End-to-end' AVF. Black arrows in the left column indicate the direction of blood flow and white arrows in the right column indicate flow separation areas. In the cross-sections, the velocity vectors show formation of Dean type vortices. Inner and outer wall position for all cases are as indicated on the cross-section (**a**) and in Figure 1c and d. Note that scale colour maps are different among end-to-side and end-to-end AVF (maximum velocity = 180 and 108 cm/s, respectively).

swing segment. Recently, in [31], OSI levels were calculated and visualized on the model surface of a side-to-side AVF. Therefore, a recommendation to future CFD studies is to perform calculation of haemodynamic wall parameters and visualization on the full surface of the AVF.

We have presented maps of OSI and RRT as indicators of disturbed flow in the three models of AVF for haemodialysis. On the inner side of the juxta-anastomosis vein in end-to-end AVF, the OSI was high (0.3), in line with the high incidence of stenosis on the swing segment [12], whereas in end-to-side AVF, the relatively low OSI (0.075) is somewhat contradictory with this evidence. Even though OSI can identify regions of flow reversal, it is insensitive to the shear stress magnitude and it seems unlikely that

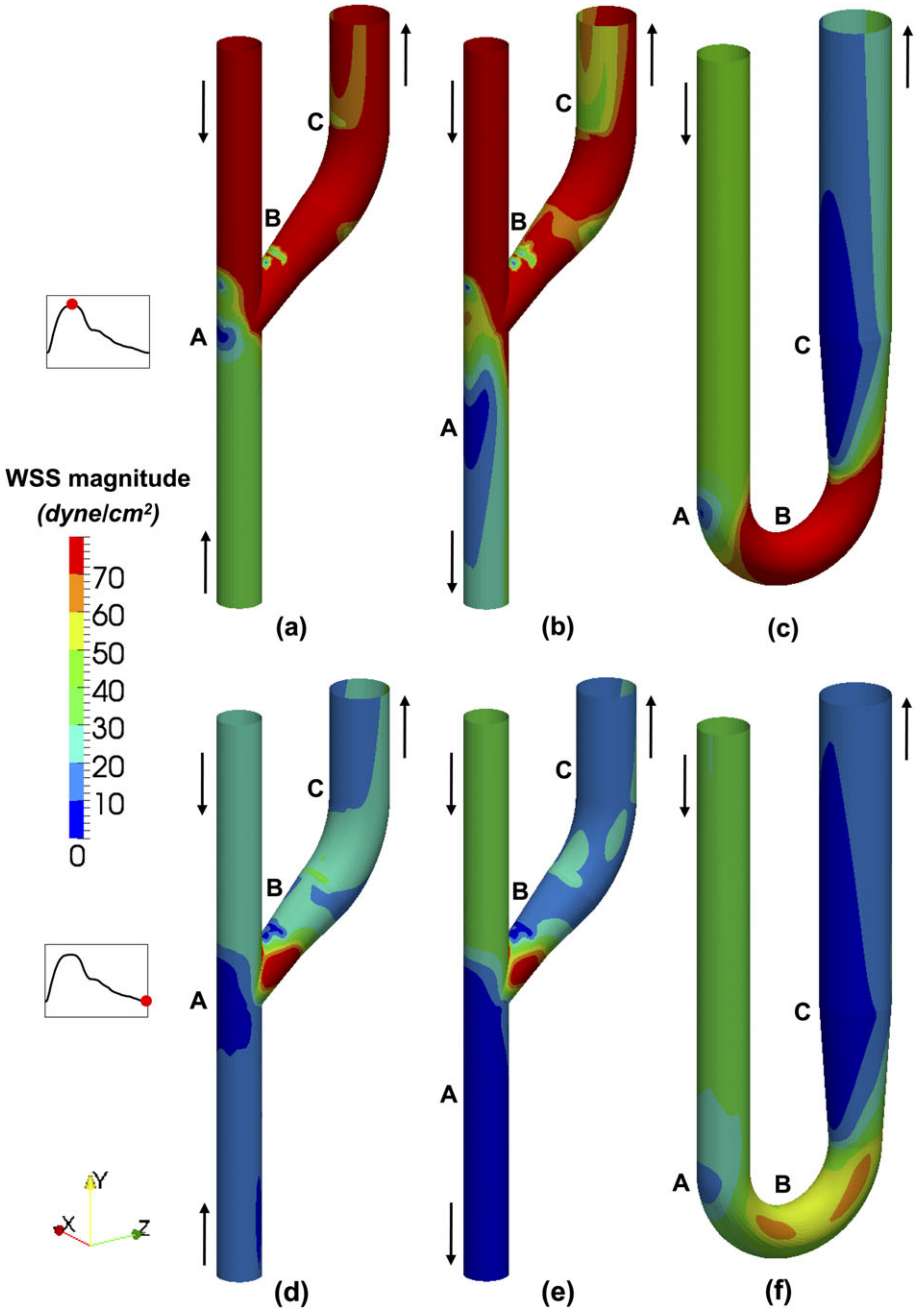

Fig. 4. WSS patterns on the AVF surface. Top and bottom rows illustrate WSS maps for maximum and minimum blood volume flow, respectively. (**a** and **d**) 'End-to-side' AVF with retrograde flow in the DA. (**b** and **e**) End-to-side AVF with antegrade flow in the DA. (**c** and **f**) 'End-to-end' AVF. High WSS zones are in red (>70 dyne/cm^2) and low WSS zones in dark blue (<10 dyne/cm^2).

endothelial cells sense OSI *per se* [40]. Instead, the RRT patterns, more extended on the swing segments due to the contribution of both oscillatory and low WSS, locate a larger portion of the sites of stenosis in end-to-side AVF. This confirms also in the AVF territory that low shear stress *per se* promotes IH, while the oscillatory shear may exacerbate the development of stenosis [8]. At the same time, OSI and RRT were higher on the anastomosis floor and on the lateral wall of DA, indicating that in end-to-side AVF, the DA limb is at risk for stenosis. This is somewhat conflicting with the current consideration that the occurrence of stenoses in the artery is low. The frequency of arterial stenoses is lower than those on venous limb, ~1.1% of all cases that rises up to 16.6% considering also the arterial anastomosis [12]. However, other studies [11, 41] reported even higher frequency up to 35%. The anastomotic floor is known as a site with high IH development in by-pass grafts anastomosis [13]. Moreover, it was shown that even if thickening of the vessel wall occurs on the arterial limb of the AVF, the stenoses are non-progressive [11] and hence lead to impairment of blood flow seldom with respect to the venous stenoses. Our finding regarding

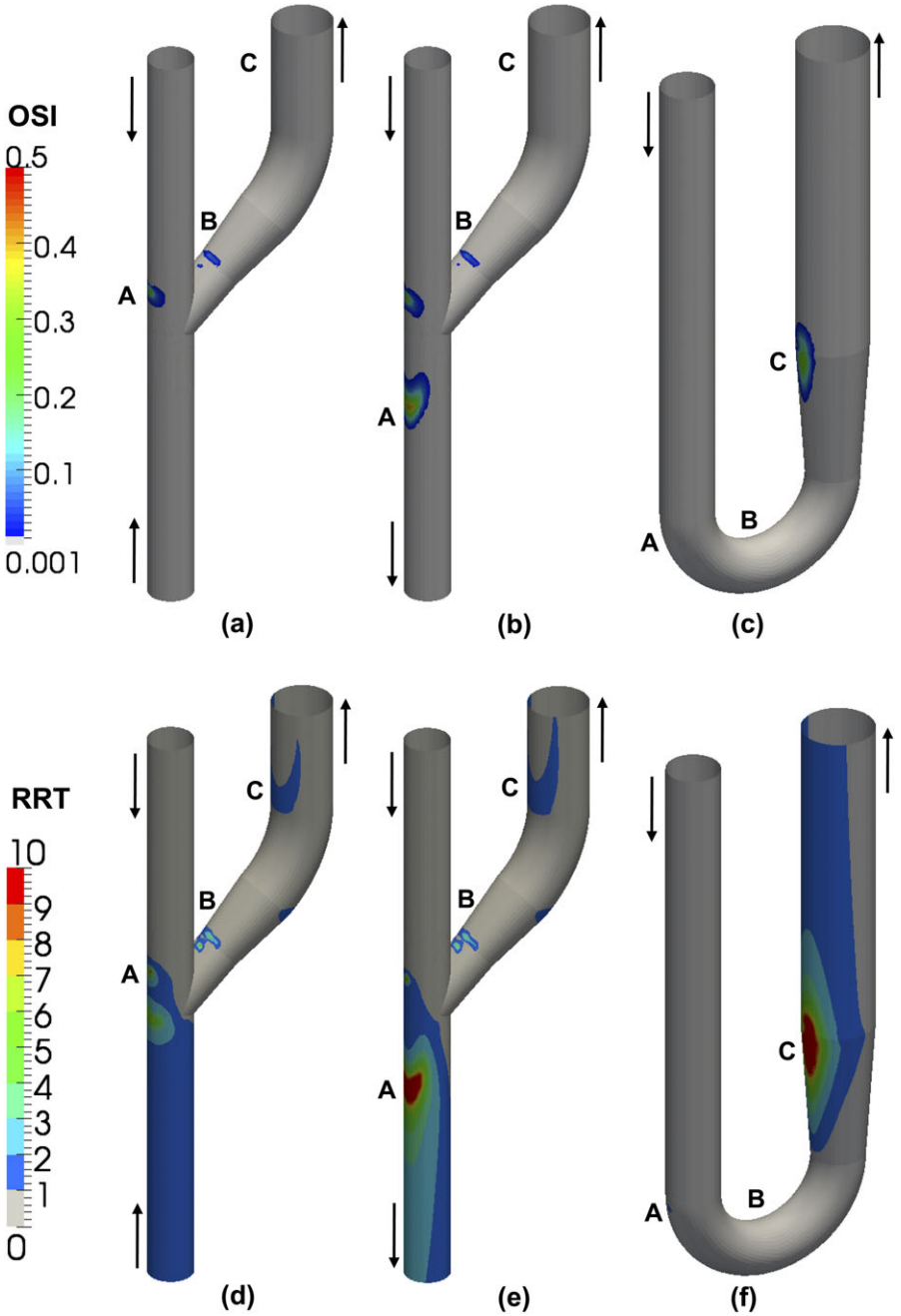

Fig. 5. Plot of OSI (**a**–**c**) and RRT (**d**–**f**) on the AVF surface. (**a** and **d**) End-to-side AVF with retrograde flow in the DA. (**b** and **e**) 'End-to-side' AVF with antegrade flow in the DA. (**c** and **f**) End-to-end AVF. OSI values <0.001 were represented in light gray to give emphasis on sites with higher OSI. RRT values <1, representing the mean of the 75% quintiles of its distributions over the mapped AVF surfaces, were represented in light gray.

highly oscillating shear on the artery and the cited evidences indicate that the mechanism of stenosis formation on the arterial side might be different from that on the venous side in AVF for haemodialysis.

On the inner wall of the outflow vein of end-to-side AVF, also known as a site at risk for IH development, OSI resulted null and also RRT was relatively low, indicating only slight influence of low WSS. Our CFD simulation in idealized AVF model did not show oscillating shear at this level of the vein. However, in real AVF, the enlargement and elongation of the vessels during the phase of the arterial remodelling may create outflow veins with sharp curvature and in this case oscillating WSS might occur.

Further studies are needed to decide the optimal haemodynamic wall parameters that better predict the sites of stenosis formation in AVF for haemodialysis. Beside OSI and RRT, which incorporates both OSI and TAWSS, other parameters that were previously proposed to quantify the haemodynamic disturbances as predictors of arterial wall sites at risk, like the WSS spatial gradient [42], the WSS temporal gradient [43] or the WSS angle gradient [44] are worth investigating in AVF patient-specific studies.

Our results on the swing segment of idealized end-to-side AVF, showing that RRT located a higher portion of the site of stenosis than OSI, support well the work of Lee *et al.* [24] on the normal carotid bifurcation, who proposed RRT as a robust single metric of low and oscillating shear. Also, in line with our observations, it has already been shown in the human coronary artery that OSI predicts well the actual site of plaque initiation, while RRT locates better the entire plaque region [45].

On the basis of our actual findings and previous experimental studies on sites of stenosis in native AVF for haemodialysis, we may speculate on the mechanisms of AVF remodelling, as illustrated in Figure 6. The VA as a whole remodels itself and matures due to the rise in blood flow rate and the augment of intraluminal pressure in the venous limb. The high flow rate induces vessel diameter enlargement through the increase in WSS and the higher pressure leads to thickening of the vessel wall that must compensate the rise of wall circumferential stress. Local wall remodelling occurs in specific sites determined by the geometry of the AVF (Points A–C in Figure 6a), where the low and oscillating WSS trigger formation of neointima, growing of intima-media thickness and successive stenosis development (Figure 6b).

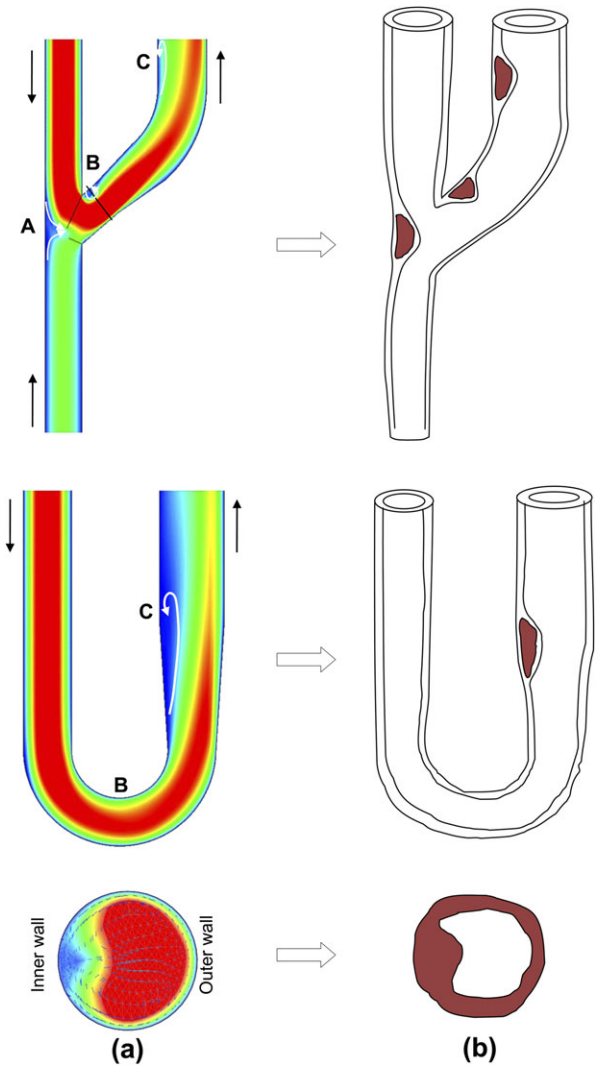

Fig. 6. Cartoon illustrating the mechanism of local AVF remodeling. (**a**) In focal sites determined by the geometry of the AVF, athero-prone haemodynamic conditions may develop. (**b**) In these areas, low and oscillating shear stresses trigger formation of neointima with subsequent increase of wall thickness and stenosis development.

The mechanism of AVF vessel thickening on the arterial limb is very likely that of IH observed in animal models of AVF [46] or in bypassed arteries [47]. It may not be excluded that atherosclerotic plaque-like formation may occur in parallel with intimal thickening even if no putative inflammatory effects from cholesterol or low density lipoprotein accumulation are present [48], especially at the anastomosis floor (Point A in Figure 6) that has WSS patterns resembling those developed at the carotid bifurcation sinus [7].

On the venous limb, the mechanism responsible of luminal occlusion is the IH in sites of low and oscillating WSS. We have shown that among blood distribution and impact on the vessel wall, the Dean flow that develops in the curved tracts of the AVF contribute to non-uniformity of WSS as well since resulting WSS is higher on lateral and lower on inner and outer wall, normal to the radius of curvature of the vessel. This undoubtedly demonstrates existence of vein sections where WSS is not uniform circumferentially even in idealized geometry of AVF. The non-uniform WSS along the circumference of the vein wall should result in non-constant intimal thickness and thus in development of eccentric stenoses. One limitation of our study is the lack of histopathology images that could directly demonstrate this hypothesis. We may, however, rely on data available in the literature on this topic. Histology of neointimal hyperplasia and its relation with WSS in stenotic AVF has been characterized in previous studies in animals [9, 49] and in subjects with AVF creation for haemodialysis [50]. The luminal shape at site of stenoses in [50] were in many cases eccentric, consistent with the hypothesis that shear stress profiles are distributed non-uniformly along the circumference of the vein. Non-uniform WSS profiles have been previously found in patient-specific CFD studies by our [25] group and others [28] in end-to-end AVF for haemodialysis. A direct demonstration of this hypothesis was made in an experimental study of end-to-side pig AVF combined with CFD in real geometries that revealed zones with non-uniform shear stress profiles circumferentially along the vein wall which correlated to a more eccentric histological pattern of intima-media thickening [49].

We found that arterial and vein walls are subjected to a haemodynamic shear stress that is much higher than the physiological shear in arteries [51] and in veins [32]. WSS was shown to remain elevated even after maturation process on the arterial side in prospective studies in patients followed up after the creation of AVF for haemodialysis [36, 52, 53]. Similar findings were reported in previous CFD studies performed in idealized geometries [27, 29] and in patient-specific investigations [25, 28, 32]. In particular, the WSS was high on the PA as well as on the outer and lateral walls of swing segments on end-to-side and on the arterial bend in end-to-end AVF. The role of chronic

exposure at high WSS was in controversial debate for years and is not yet clearly understood. Earlier studies [54, 55] considered that levels of high shear stress may lead to endothelial layer degeneration and erosion. On the contrary, more recent studies elucidated that chronic exposure to high levels of WSS with little temporal fluctuations has beneficial effects by promoting an athero-protective phenotype [56–58]. Overall, high shear stress resulting from the high flow and higher venous pressure stimuli will elicit arterial and vein remodelling by promoting cell proliferation [59]. Locally, on one hand, high WSS protects against neointima formation, but on the other hand, high WSS spatial gradients may alter the functional state of the endothelial layer and probably that of underlying smooth muscle cell layer [60, 61]. Furthermore, little is known about the vein endothelium that is subjected to even higher gradient regimes of WSS after AVF creation considering that in the pre-operative condition vein physiological range of WSS is about 1–6 dyne/cm^2 [7, 32].

In the present work, we only took into account the radiocephalic native fistula created at the wrist in an end-to-side and end-to-end manner. Other types of VA, like the upper arm fistulae or arteriovenous grafts should be treated in further studies considering their different geometry and flow conditions. We used idealized geometry and imposed realistic pulsatile boundary conditions in order to catch the general flow features that develop in the AVF soon after the surgical creation. While in patient-specific studies, the variability of the AVF geometry in terms of bends, torsion and luminal area variation will reflect the haemodynamic condition of the single subject; in our opinion, the present study may well represent the general flow behaviour and common shear stress patterns in these two types of radial-cephalic AVF. The computational modelling of AVF provides vantages such as the possibility to simulate different geometries and a variety of flow conditions. For example, it was shown that the geometry of an out-of-plane respect to a planar graft strongly influences perianastomotic WSS patterns by breaking the Dean vortices symmetry [62]. Also, in helically sinuous vascular prostheses, it was demonstrated that the curvature and torsion affect the flow field in terms of axial velocity, WSS and vorticity [63] and more importantly, the Dean vortices produced by the curvature are changed by the torsion to a predominantly single vortex, with consequent changes of WSS patterns. This type of CFD modelling should be employed in upcoming studies in idealized AVF to better understand how the anastomotic angle or vein torsion, that in part may be amenable to surgical manipulation, would impact on the local WSS patterns and targeted towards the lowering of RRT. At the next level, these studies may be performed in patient-specific pilot studies, aimed at minimizing the AVF failure by reducing the venous development of neointimal hyperplasia.

In conclusion, by using unsteady CFD modelling in radial-cephalic AVF created at the wrist, we have found that, as contributing factors of the pathogenesis of IH, the localization of low and oscillating haemodynamic shear in the post-operative flow condition may explain the preferential localization of the stenosis. Despite being exposed to a sudden increase in flow rate, sites of disturbed flow with low and oscillating WSS in AVF occur in focal sites driven by the vessel geometry and the blood flow distribution.

Acknowledgements. The study was partially funded by the 7th Framework Programme of the European Commission (FP7-ICT-2007-2 ARCH Project, grant agreement nr. 224390).

Conflict of interest statement. None declared.

References

1. Brescia MJ, Cimino JE, Appel K *et al.* Chronic hemodialysis using venipuncture and a surgically created arteriovenous fistula. *N Engl J Med* 1966; 275: 1089–1092
2. Besarab A, Ravani P, Spergel LM *et al.* The native arteriovenous fistula in 2007. Research needs. *J Nephrol* 2007; 20: 668–673
3. Asif A, Roy-Chaudhury P, Beathard GA. Early arteriovenous fistula failure: a logical proposal for when and how to intervene. *Clin J Am Soc Nephrol* 2006; 1: 332–339
4. Roy-Chaudhury P, Spergel LM, Besarab A *et al.* Biology of arteriovenous fistula failure. *J Nephrol* 2007; 20: 150–163
5. Konner K. The initial creation of native arteriovenous fistulas: surgical aspects and their impact on the practice of nephrology. *Semin Dial* 2003; 16: 291–298
6. Konner K. History of vascular access for haemodialysis. *Nephrol Dial Transplant* 2005; 20: 2629–2635
7. Malek AM, Alper SL, Izumo S. Hemodynamic shear stress and its role in atherosclerosis. *JAMA* 1999; 282: 2035–2042
8. Davies PF. Hemodynamic shear stress and the endothelium in cardiovascular pathophysiology. *Nat Clin Pract Cardiovasc Med* 2009; 6: 16–26
9. Sho E, Nanjo H, Sho M *et al.* Arterial enlargement, tortuosity, and intimal thickening in response to sequential exposure to high and low wall shear stress. *J Vasc Surg* 2004; 39: 601–612
10. Diskin CJ, Stokes TJ, Dansby LM *et al.* Understanding the pathophysiology of hemodialysis access problems as a prelude to developing innovative therapies. *Nat Clin Pract Nephrol* 2008; 4: 628–638
11. Sivanesan S, How TV, Bakran A. Sites of stenosis in AV fistulae for haemodialysis access. *Nephrol Dial Transplant* 1999; 14: 118–120
12. Badero OJ, Salifu MO, Wasse H *et al.* Frequency of swing-segment stenosis in referred dialysis patients with angiographically documented lesions. *Am J Kidney Dis* 2008; 51: 93–98
13. Haruguchi H, Teraoka S. Intimal hyperplasia and hemodynamic factors in arterial bypass and arteriovenous grafts: a review. *J Artif Organs* 2003; 6: 227–235
14. Girerd X, London G, Boutouyrie P *et al.* Remodeling of the radial artery in response to a chronic increase in shear stress. *Hypertension* 1996; 27: 799–803
15. Corpataux JM, Haesler E, Silacci P *et al.* Low-pressure environment and remodelling of the forearm vein in Brescia-Cimino haemodialysis access. *Nephrol Dial Transplant* 2002; 17: 1057–1062
16. Ku DN, Giddens DP, Zarins CK *et al.* Pulsatile flow and atherosclerosis in the human carotid bifurcation. *Arteriosclerosis* 1985; 5: 293–302
17. Perktold K, Nerem RM, Peter RO. A numerical calculation of flow in a curved tube model of the left main coronary artery. *J Biomech* 1991; 24: 175–189
18. Moore JEJ, Xu C, Glagov S *et al.* Fluid wall shear stress measurements in a model of the human abdominal aorta: oscillatory behavior and relationship to atherosclerosis. *Arteriosclerosis* 1994; 110: 225–240
19. Moore JEJ, Ku DN. Pulsatile velocity measurements in a model of the human abdominal aorta under resting conditions. *J Biomech Eng* 1994; 116: 337–346
20. Steinman DA, Vinh B, Ross Ethier C *et al.* A numerical simulation of flow in a two-dimensional end-to-side anstomosis model. *J Biomech Eng* 1993; 115: 112–118

21. Ethier CR, Steinman DA, Zhang X *et al.* Flow waveform effects on end-to-side anastomotic flow patterns. *J Biomech* 1998; 31: 609–617
22. Zarins CK, Giddens DP, Bharadvaj BK. Carotid bifurcation atherosclerosis: quantitative correlation of plaque localization with flow velocity profiles and wall shear stress. *Circ Res* 1983; 53: 502–514
23. He X, Ku DN. Pulsatile flow in the human left coronary artery bifurcation: average conditions. *J Biomech Eng* 1996; 118: 74–82
24. Lee SW, Antiga L, Steinman DA. Correlations among indicators of disturbed flow at the normal carotid bifurcation. *J Biomech Eng* 2009; 131: 061013
25. Ene-Iordache B, Mosconi L, Remuzzi G *et al.* Computational fluid dynamics of a vascular access case for hemodialysis. *J Biomech Eng* 2001; 123: 284–292
26. Krueger U, Zanow J, Scholz H. Computational fluid dynamics and vascular access. *Artif Organs* 2002; 26: 571–575
27. Van Tricht I, De Wachter D, Tordoir J *et al.* Comparison of the hemodynamics in 6mm and 4-7 mm hemodialysis grafts by means of CFD. *J Biomech* 2006; 39: 226–236
28. Kharboutly Z, Fenech M, Treutenaere JM *et al.* Investigations into the relationship between hemodynamics and vascular alterations in an established arteriovenous fistula. *Med Eng Phys* 2007; 29: 999–1007
29. Van Canneyt K, Pourchez T, Eloot S *et al.* Hemodynamic impact of anastomosis size and angle in side-to-end arteriovenous fistulae: a computer analysis. *J Vasc Access* 2010; 11: 52–58
30. Kharboutly Z, Deplano V, Bertrand E *et al.* Numerical and experimental study of blood flow through a patient-specific arteriovenous fistula used for hemodialysis. *Med Eng Phys* 2010; 32: 111–118
31. Niemann AK, Udesen J, Thrysoe S *et al.* Can sites prone to flow induced vascular complications in a-v fistulas be assessed using computational fluid dynamics? *J Biomech* 2010; 43: 2002–2009
32. Carroll GT, McGloughlin TM, Burke PE *et al.* Wall shear stresses remain elevated in mature arteriovenous fistulas: a case study. *J Biomech Eng* 2011; 133: 021003
33. NKF-K/DOQI Clinical Practice Guidelines for Vascular Access: update 2000. *Am J Kidney Dis* 2001; 37: S137–S181
34. Berardinelli L. The endless history of vascular access: a surgeon's perspective. *J Vasc Access* 2006; 7: 103–111
35. Konner K. The anastomosis of the arteriovenous fistula–common errors and their avoidance. *Nephrol Dial Transplant* 2002; 17: 376–379
36. Ene-Iordache B, Mosconi L, Antiga L *et al.* Radial artery remodeling in response to shear stress increase within arteriovenous fistula for hemodialysis access. *Endothelium* 2003; 10: 95–102
37. Sivanesan S, How TV, Black RA *et al.* Flow patterns in the radiocephalic arteriovenous fistula: an in vitro study. *J Biomech* 1999; 32: 915–925
38. Sivanesan S, How TV, Bakran A. Characterizing flow distributions in AV fistulae for haemodialysis access. *Nephrol Dial Transplant* 1998; 13: 3108–3110
39. Gijsen FJH, Brands PJ, van de Vosse FN *et al.* Assessment of wall shear rate measurements with ultrasound. *J Vasc Invest* 1998; 4: 187–196
40. Himburg HA, Grzybowski DM, Hazel AL *et al.* Spatial comparison between wall shear stress measures and porcine arterial endothelial permeability. *Am J Physiol Heart Circ Physiol* 2004; 286: H1916–H1922
41. Asif A, Gadalean FN, Merrill D *et al.* Inflow stenosis in arteriovenous fistulas and grafts: a multicenter, prospective study. *Kidney Int* 2005; 67: 1986–1992
42. Lei M, Kleinstreuer C, Truskey GA. A focal stress gradient-dependent mass transfer mechanism for atherogenesis in branching arteries. *Med Eng Phys* 1996; 18: 326–332
43. Ojha M. Wall shear stress temporal gradient and anastomotic intimal hyperplasia. *Circ Res* 1994; 74: 1227–1231
44. Longest PW, Kleinstreuer C. Computational haemodynamics analysis and comparison study of arterio-venous grafts. *J Med Eng Technol* 2000; 24: 102–110
45. Knight J, Olgac U, Saur CS *et al.* Chosing the optimal wall shear parameter for the prediction of placque location—a patient-specific computational study in human right coronary arteries. *Atherosclerosis* 2010; 211: 445–450
46. Fan Y, Xu Z, Jiang W *et al.* An S-type bypass can improve the hemodynamics in the bypassed arteries and suppress intimal hyperplasia along the host artery floor. *J Biomech* 2008; 41: 2498–2505
47. Migliavacca F, Dubini G. Computational modeling of vascular anastomoses. *Biomech Model Mechanobiol* 2005; 3: 235–250
48. Sloop GD, Fallon KB, Zieske AW. Atherosclerotic plaque-like lesions in synthetic arteriovenous grafts: implications for atherogenesis. *Atherosclerosis* 2002; 160: 133–139
49. Krishnamoorthy MK, Banerjee RK, Wang Y *et al.* Hemodynamic wall shear stress profiles influence the magnitude and pattern of stenosis in a pig AV fistula. *Kidney Int* 2008; 74: 1410–1419
50. Roy-Chaudhury P, Arend L, Zhang J *et al.* Neointimal hyperplasia in early arteriovenous fistula failure. *Am J Kidney Dis* 2007; 50: 782–790
51. Dammers R, Stifft F, Tordoir JH *et al.* Shear stress depends on vascular territory: comparison between common carotid and brachial artery. *J Appl Physiol* 2003; 94: 485–489
52. Dammers R, Tordoir JH, Welten RJ *et al.* The effect of chronic flow changes on brachial artery diameter and shear stress in arteriovenous fistulas for hemodialysis. *Int J Artif Organs* 2002; 25: 124–128
53. Dammers R, Tordoir JH, Kooman JP *et al.* The effect of flow changes on the arterial system proximal to an arteriovenous fistula for hemodialysis. *Ultrasound Med Biol* 2005; 31: 1327–1333
54. Fry DL. Acute vascular endothelial changes associated with increased blood velocity gradients. *Circ Res* 1968; 22: 165–197
55. Langille BL, Reidy MA, Kline RL. Injury and repair of endothelium at sites of flow disturbances near abdominal aortic coarctations in rabbits. *Arteriosclerosis* 1986; 6: 146–154
56. Caro CG, Fitz-Gerald JM, Schroter RC. Atheroma and arterial wall shear. Observation, correlation and proposal of a shear dependent mass transfer mechanism for atherogenesis. *Proc R Soc Lond B Biol Sci* 1971; 177: 109–159
57. Davies PF. Flow-mediated endothelial mechanotransduction. *Physiol Rev* 1995; 75: 519–560
58. Traub O, Berk BC. Laminar shear stress: mechanisms by which endothelial cells transduce an atheroprotective force. *Arterioscler Thromb Vasc Biol* 1998; 18: 677–685
59. Sho E, Komatsu M, Sho M *et al.* High flow drives vascular endothelial cell proliferation during flow-induced arterial remodeling associated with the expression of vascular endothelial growth factor. *Exp Mol Pathol* 2003; 75: 1–11
60. DePaola N, Gimbrone MA Jr, Davies PF *et al.* Vascular endothelium responds to fluid shear stress gradients. *Arterioscler Thromb* 1992; 12: 1254–1257
61. DePaola N, Davies PF, Pritchard WFJ *et al.* Spatial and temporal regulation of gap junction connexin43 in vascular endothelial cells exposed to controlled disturbed flows in vitro. *Proc Natl Acad Sci U S A* 1999; 96: 3154–3159
62. Papaharilaou Y, Doorly DJ, Sherwin SJ. The influence of out-of-plane geometry on pulsatile flow within a distal end-to-side anastomosis. *J Biomech* 2002; 35: 1225–1239
63. Lee KE, Lee JS, Yoo JY. A numerical study on steady flow in helically sinuous vascular prostheses. *Med Eng Phys* 2010; 33: 38–46

Received for publication: 22.10.10; Accepted in revised form: 16.5.11